

# Dynamic analysis of a buckled asymmetric piezoelectric beam for energy harvesting

Louis Van Blarigan<sup>a)</sup> and Jeff Moehlis

Department of Mechanical Engineering, University of California, Santa Barbara, California 93106, USA

(Received 3 November 2015; accepted 22 February 2016; published online 9 March 2016)

A model of a buckled beam energy harvester is analyzed to determine the phenomena behind the transition between high and low power output levels. It is shown that the presence of a chaotic attractor is a sufficient condition to predict high power output, though there are relatively small areas where high output is achieved without a chaotic attractor. The chaotic attractor appears as a product of a period doubling cascade or a boundary crisis. Bifurcation diagrams provide insight into the development of the chaotic region as the input power level is varied, as well as the intermixed periodic windows. © 2016 AIP Publishing LLC. [<http://dx.doi.org/10.1063/1.4943172>]

**Vibrational energy harvesting allows small amounts of power to be extracted from the environment or a device's operation. Capturing this energy can provide a power source for small electronic devices without the need for batteries or external power supplies, thus potentially reducing installation and maintenance costs. This article provides a detailed dynamical systems analysis of a model for a buckled beam vibrational energy harvester, identifying transitions to chaos and other bifurcations which lead to high energy output over a range of vibration frequencies. Such an analysis will be useful for determining if a parameter change in the system design results in increased bandwidth for high energy output, an important step for system optimization.**

which requires that the beam pass through the unstable central equilibrium position in a straight configuration, invalidating the small strain assumption if the transverse displacements are even moderately large in comparison to the dimensions of the beam.<sup>4</sup> Some dynamic analysis of this type of model has been done,<sup>2</sup> but the authors cite these as *proof of concept* models and do not attempt to make accurate identifications of the underlying cause of bifurcations, leaving this as an area requiring further investigation.

Recently, a model has been generated<sup>4</sup> which demonstrates reasonable and conservative agreement with an experimental device in both power output and bandwidth, while also agreeing well with qualitative examinations of the behavior in different regimes around the high power output region. Providing a detailed dynamic analysis of the transitions to relatively high power output can help provide understanding about why these transitions occur and provide a framework for optimizing the output power in response to a known vibration source. The beam under investigation is constructed by the union of a bimorph piezoelectric beam and a single layer piezoelectric beam, both available commercially from Advanced Ceramics.<sup>5</sup> The joint is glued with approximately 10 mm of overlap, and both ends are clamped to prevent rotation or displacement in relation to the clamping surface. The mounts are then moved closer together than the natural length of the beam until a buckled state is realized. The entire structure is then subjected to a vibration in a direction perpendicular to the mounting surfaces. A sketch demonstrating the fundamental beam construction is shown in Figure 1. Additional details of the experimental setup and methods can be found in Ref. 6.

In the present paper, examinations are made of the transitions between single well and double well behavior, including identification and tracing of the responsible bifurcation branches. Several methods are used, including time averages, Poincaré maps, bifurcation diagrams, and numerical bifurcation analysis to specifically identify types and locations of bifurcations. The transition to high power output is found to be closely related to this transition between single well and double well behavior, but there are regions where relatively

## I. INTRODUCTION

Harvesting energy from ambient vibrational energy sources using piezoelectric beams is an area of much current interest, as can be seen from the multitude of recent articles regarding such devices as reviewed in Ref. 1. These devices can be used to provide an energy source in environments where running power lines or replacing batteries is not a practical option. Though conversion efficiencies are typically quite small, i.e., milliwatt power generation from watts of vibrational energy, scavenging any otherwise wasted energy is a worthwhile pursuit. Often, energy harvesting devices are designed as linear resonant devices, which are only capable of harvesting energy from a very narrow bandwidth of excitation frequencies.<sup>13</sup> Increasing the bandwidth of excitation frequencies from which the device can extract energy can offer a significant improvement in response to time varying signals. Buckled beams characterized by a double well potential have been utilized by many researchers to broaden the bandwidth of energy output as compared to devices which display linear resonance. Simple models demonstrating bi-stability and chaotic response have been demonstrated,<sup>2,3</sup> but typically these models are developed from a single mode Galerkin Projection

<sup>a)</sup>louis01@umail.ucsb.edu

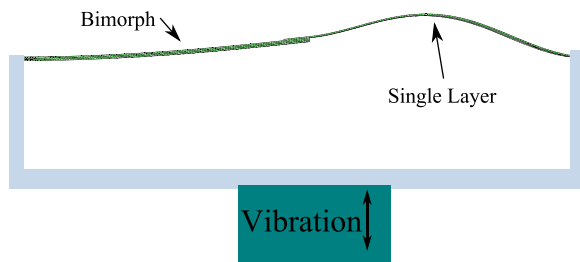


FIG. 1. A sketch of the beam demonstrating the construction, direction of vibration, and approximate buckled shape. The stiffer bimorph beam is on the left, and the single layer beam is on the right. The beam is clamped in a fixture, and vibrated in the plane of the page, assuming that any motion in and out of the page is negligible.

high power output is achieved without snap-through behavior between the wells, and the underlying cause of this phenomenon is also examined.

## II. MODEL GENERATION

For simplicity, our analysis of the model from Ref. 4 deals with sinusoidal excitations. Due to the complexity of the system, analytic modes are not available about the nonlinear buckled equilibrium state,<sup>4</sup> so finite element analysis was used to determine mode shapes. The Green-Lagrange strain tensor was used to approximate the axial strain under assumptions of small strain and moderate rotation, with the dependent variables as the mode amplitudes. From this, an Euler-Lagrange energy function was developed and used to construct equations of motion based on the mode amplitudes. The primary shape mode is called the equilibrium mode, and named “ $a_0$ ,” which is defined as having amplitude  $\pm 1$  at the equilibrium positions, with all other modes equal to zero. The presence of two equilibrium positions gives the system a double well character, which is exploited to increase the bandwidth compared to a single well system. Three additional vibrational modes were defined to complete the basis for projecting the beam dynamics onto. Deriving a model using a buckled equilibrium shape plus the first three mode shapes, we found equations of the form

$$\begin{aligned} \ddot{a}_{i-1} = & b_{(i,1)} a_0 + b_{(i,2)} a_0^3 + b_{(i,3)} a_1 + b_{(i,4)} a_0 a_1^2 + b_{(i,5)} a_1^3 \\ & + b_{(i,6)} a_2 + b_{(i,7)} a_0 a_1 a_2 + b_{(i,8)} a_1^2 a_2 + b_{(i,9)} a_0 a_2^2 \\ & + b_{(i,10)} a_1 a_2^2 + b_{(i,11)} a_2^3 + b_{(i,12)} a_3 + b_{(i,13)} a_0 a_1 a_3 \\ & + b_{(i,14)} a_1^2 a_3 + b_{(i,15)} a_0 a_2 a_3 + b_{(i,16)} a_2^2 a_3 \\ & + b_{(i,17)} a_0 a_3^2 + b_{(i,18)} a_1 a_2^2 + b_{(i,19)} a_2 a_3^2 + b_{(i,20)} a_3^3 \\ & + b_{(i,21)} A \omega^2 \sin \omega t + b_{(i,22)} v_B + b_{(i,23)} a_0 v_S \\ & + b_{(i,24)} a_1 v_S + b_{(i,25)} a_2 v_S + b_{(i,26)} a_3 v_S \\ & + b_{(i,27)} \dot{a}_0 + b_{(i,28)} \dot{a}_1 + b_{(i,29)} \dot{a}_2 + b_{(i,30)} \dot{a}_3, \end{aligned} \quad (1)$$

$$\dot{v}_B = d_0 \dot{a}_0 + d_1 \dot{a}_1 + d_2 \dot{a}_2 + d_3 \dot{a}_3 + d_4 v_B, \quad (2)$$

$$\begin{aligned} \dot{v}_S = & \dot{a}_0 (h_0 a_0 + h_1 a_1 + h_2 a_2 + h_3 a_3) \\ & + \dot{a}_1 (h_4 a_0 + h_5 a_1 + h_6 a_2 + h_7 a_3) \\ & + \dot{a}_2 (h_8 a_0 + h_9 a_1 + h_{10} a_2 + h_{11} a_3) \\ & + \dot{a}_3 (h_{12} a_0 + h_{13} a_1 + h_{14} a_2 + h_{15} a_3) + h_{16} v_S, \end{aligned} \quad (3)$$

where  $b$  is a matrix of coefficients with as many rows as shape functions,  $d$  and  $h$  are vectors of coefficients, and  $i$  runs from 1 to 4. The parameters  $\omega$ ,  $A$ ,  $v_B$ , and  $v_S$  are the forcing frequency in radians/s, excitation amplitude, voltage in the bimorph section, and voltage in the single layer beam, respectively. Further details about the model generation are presented in Ref. 4.

## III. ANALYSIS OF THE MODEL

We propose that the critical parameters for examining a nonlinear energy harvesting system are the forcing power level and the frequency and/or bandwidth of excitation. Commonly, comparisons are made using the amplitude of the acceleration of the forcing signal, without regard to the fact that the forcing power level is not constant or linear as the frequency is changed when the acceleration amplitude is kept constant. This results in higher frequency tests being done at significantly higher forcing power levels which can skew the results to appear that the device works just as well or better at higher frequencies, particularly damaging the perception of output bandwidth. The lack of superposition in nonlinear devices compounds this phenomenon. Sweeps at constant acceleration often result in overlapping power levels with another sweep which is presented as a separate result, and interpolation or normalization are not possible. Only comparing signals produced by the same input power level allows for a fair comparison of output root mean squared (RMS) values without any skew based on frequency of excitation.

To begin examination of the model, we produce a plot of power output over the parameter space of frequency and available forcing power. This can be seen in Figure 2. Here, the forcing power is calculated as the forcing amplitude squared multiplied with the forcing frequency in radians/second cubed. This represents the maximum amplitude of the acceleration multiplied with the maximum value of the velocity, providing a measure of mechanical power. Though these quantities are never at their maxima at the same instant, it provides a consistent and easily calculable reference for which to compare forcing power levels, which we will denote as the available input power. The output power is the sum of the RMS voltage output divided by the resistive load in kilo-ohms for both the single layer and bimorph sections of the beam.

Note that there is a region of the parameter space where the power output is significantly higher. This region begins at approximately 5 W of available input power and a forcing frequency of 41 Hz, where the bandwidth is quite small. As the available input power is increased, there is a significant increase of the bandwidth of the high power region. Interestingly, around 7 W of available input power there is a region where the bandwidth shrinks. This phenomenon is due to the existence of a non-attracting set of high power orbits that settles to a small amplitude orbit after a period of high power transients, as will be shown in more detail later in this paper. The high power region is associated with the beam entering into a behavior which transitions between the two stable equilibria of the buckled beam, which we will call a snap-through behavior. The region of parameter space where the beam exhibits this snap-through behavior can be determined

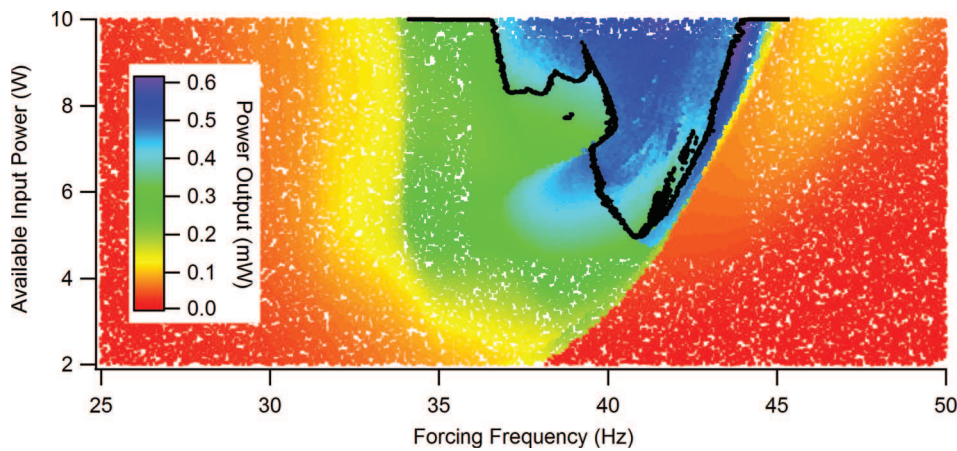


FIG. 2. Summed RMS power output in mW of both single layer beam and bimorph beam. Note the sharp transition between low and high power on the high frequency side of the tongue. Also note the “bite” that seems to be taken out of the high power region on the low frequency side. The black line indicates a transition between single well and double well behavior, demonstrating that snap-through is typically associated with relatively high power output.

by examining the long-time average of the amplitude of the equilibrium mode.<sup>7</sup> When the beam is settled into single well behavior, the time average is very close to positive or negative one, while during snap-through behavior the time average approaches zero. The black trace in Figure 2 represents the boundary of the region where the snap-through behavior represents the attracting set, and all orbits inside the region make well-to-well transitions. Note that while this encompasses a large portion of the high power region, there is a significant slice on the high frequency side where high power output is realized without snap-through behavior, as well as a small lobe on the low frequency side. These regions will be examined later in the paper.

We note that there are small regions of this parameter space where multiple stable trajectories exist, generally having different levels of power output. These regions are narrow bands near the transition between low and high power output which can be accessed by choosing appropriate initial conditions. However, these regions are small enough in comparison to the parameter space that they make no significant difference in the visualization of the power output. Once the system has transitioned to snap-through behavior, randomly chosen initial conditions demonstrate convergence to the high power attractor. Global stability cannot be guaranteed, due to the small strain assumption used to generate the model. If the mode amplitudes get large enough, this assumption will be invalidated and any results obtained from this model will be invalid.

### A. Bifurcation diagrams

For a specified available input power level, a bifurcation diagram can be created. To do so, a range of frequencies is selected with adequate density to catch interesting phenomena, and a time series is run at each chosen excitation frequency. After discarding any transient portion, a Poincaré section is created by strobing the time series once per forcing period. Selecting one representative function and plotting the amplitude of that function across the frequency range, a bifurcation diagram is generated; see Figure 3. For this example, an available input power level of 6 W has been selected, and the function we are examining is the amplitude of the equilibrium mode,  $a_0$ . Periodic behavior is expected to have all of the Poincaré iterates lie on top of each other, and are therefore

expected to correspond to a point or a well defined set of points at the respective frequency. Beginning at the far right of the diagram, a period one oscillation is noted for which a demonstrative time series can be seen in Figure 4(a). Decreasing the forcing frequency results in this behavior splitting into a period two oscillation, as seen in Figure 4(b), suggesting the existence of a period doubling cascade, which will be examined shortly. Moving further down in frequency, chaotic response is found first in just one well, panel (c), then the attractor expands until it fills the well, then snap-through behavior begins with the attractor visiting both wells indiscriminately, see panel (d). This behavior suggests that the transition from single well behavior to snap-through behavior is governed by an *attractor merging crisis*<sup>8</sup> of the symmetry related attractors in each well. Traveling for a while through the chaotic zone, suddenly a periodic window is encountered. A time series with Poincaré map can be seen in panel (e) of Figure 4. Further reduction in frequency carries us through several more chaotic zones and periodic windows before we return to a period one oscillation.

Note that at approximately 42.7 Hz in Figure 3 there is a discontinuity in the bifurcation branch of the period one orbit. To determine the cause of this irregularity, we can use the numerical bifurcation software AUTO<sup>9</sup> to follow the development of the period one orbit as we move through this range of forcing frequencies. We will start on the stable period one orbit above the discontinuity and follow the orbit as the forcing frequency is decreased. We find that there is a region where multiple saddle-node bifurcations create multiple stable orbits. Figure 5 shows the evolution of the orbit through this frequency range. The red portions of the trace are the unstable branch of the period one orbit, while the blue portions are stable. The vertical axis represents the  $L^2$  norm of the voltage produced by this orbit, so higher values are associated with higher power output. We note that between 42.39 and 42.71 Hz, there are multiple stable instances of this period one orbit, connected through 4 saddle-node bifurcations (marked with black triangles on the figure). While the intermediate stable orbit is not easily discovered with a time series exploration, the low power and high power branches are both easily observed, and the switch between them is what causes the discontinuity observed in Figure 3. Moreover, this jump between stable orbits is the cause of the

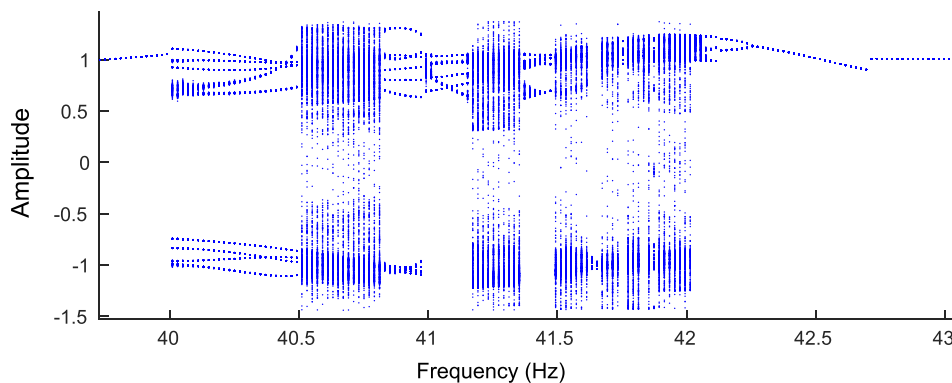


FIG. 3. Bifurcation diagram created by strobing the system at the forcing frequency. The selected function is the equilibrium amplitude  $a_0$ , and the available input power is 6 W. Frequencies with well defined discrete points have periodic solutions, while frequencies where the Poincaré intersections fill in vertical bands of parameter space are chaotic.

sudden jump in output power noted at the high frequency side of the high power region in Figure 2. The stable high power branch of the orbit does not exist for long before it loses stability at a period doubling bifurcation (such bifurcations are marked with black squares). The period doubled stable solution can be traced to a second period doubling bifurcation, where a new branch leads to a third bifurcation, and quickly the orbit becomes too complex and the bifurcations too close together to identify any further, accumulating at approximately 42.075 Hz. Recall that the Feigenbaum number ( $\delta$ ) can be calculated as

$$\lim_{n \rightarrow \infty} \frac{\lambda_n - \lambda_{n-1}}{\lambda_{n+1} - \lambda_n} = \delta \rightarrow 4.6692016,$$

where  $\lambda_n$  represents the frequency at which the  $n$ th bifurcation occurs.<sup>10,11</sup> For the present model, this is calculated as 4.5 for the fourth period doubling bifurcation ( $n=4$ ), which is reasonably close to the Feigenbaum number, suggesting that this period doubling cascade obeys the universal scaling expected of a period doubling transition to chaotic behavior.

The period one orbit can be traced through the high power region, where it remains unstable, until stability is regained as we drop back into single well oscillations near a saddle-node bifurcation on the low frequency side of the high power region, corresponding to 39.6 Hz with 6 W of available input power. The saddle-node bifurcation appears to trace the boundary, as can be seen in Figure 7, along the low frequency side of the snap-through region. However, this bifurcation branch is not responsible for the transition. There is a very small region where both the stable period one orbit, which undergoes the saddle-node bifurcation, and the chaotic attractor coexist. A time series including the transient portion can be seen in Figure 6. The transient portion produces snap-through behavior in a manner similar to trajectories where snap-through is the attracting behavior. The overlap of stable period one and chaotic regions combined with the presence of transient chaos indicates that an unstable orbit has collided with the chaotic attractor, creating a boundary crisis.<sup>12</sup> The chaotic set becomes non-attracting, but orbits near the boundary are able to jump onto this set for a short period of time

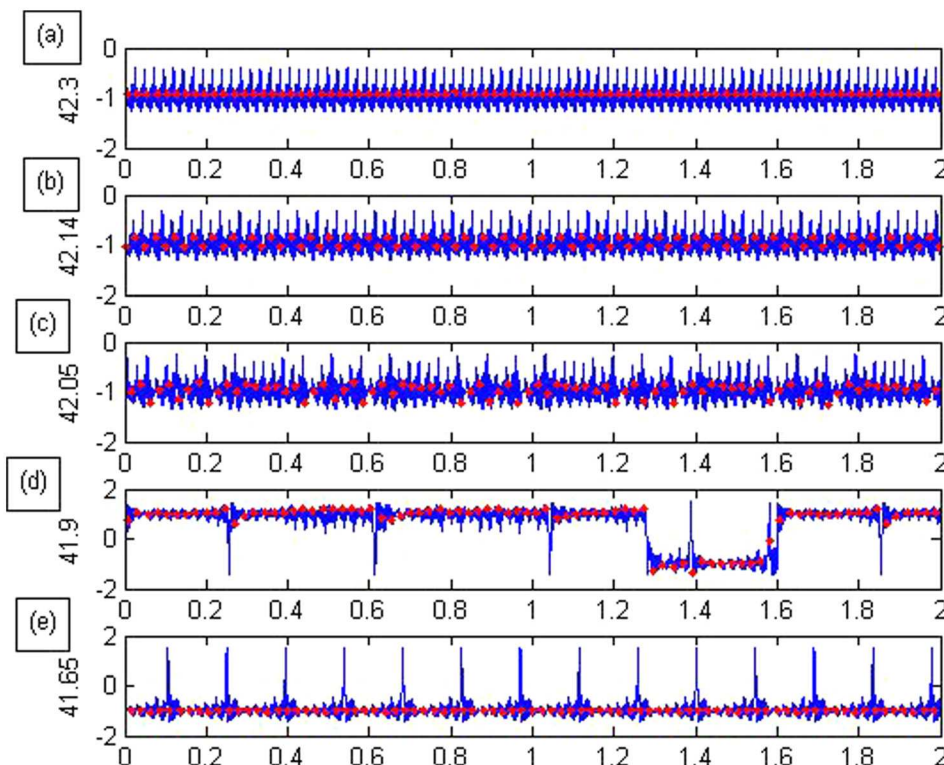


FIG. 4. A set of time series demonstrating qualitatively different behaviors. All plots are of the equilibrium mode amplitude, with red dots overlaid at the Poincaré sections used to create the bifurcation diagrams. Panel (a) demonstrates a simple period 1 orbit which exists at 42.3 Hz. As the frequency is decreased to 42.14 Hz, the orbit becomes period 2, as seen in panel (b). Chaos is first noted in a single well, as shown in panel (c) at 42.05 Hz. Quickly this chaotic attractor merges with the attractor existing in the other well, and snap-through behavior is noted, as seen in panel (d) at 41.9 Hz. Moving down in forcing frequency through the chaotic zone, a periodic window is encountered, as seen in panel (e) at 41.65 Hz.

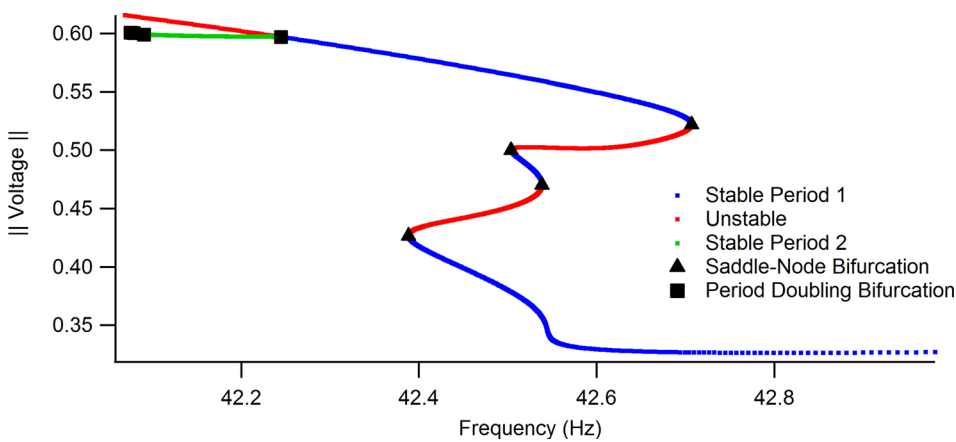


FIG. 5. Evolution of the period one orbit at the high frequency side of the high power region. Blue traces indicate regions of stability of the period one orbit; the green trace is a stable period two orbit, while the red lines indicate unstable branches. Saddle node bifurcations are marked with black triangles, while period doubling bifurcations are marked with black squares. The existence of multiple stable orbits at different power output levels provides insight to the sudden change of output power observed here. The period doubling cascade at the far left of the figure indicates the transition to chaotic behavior.

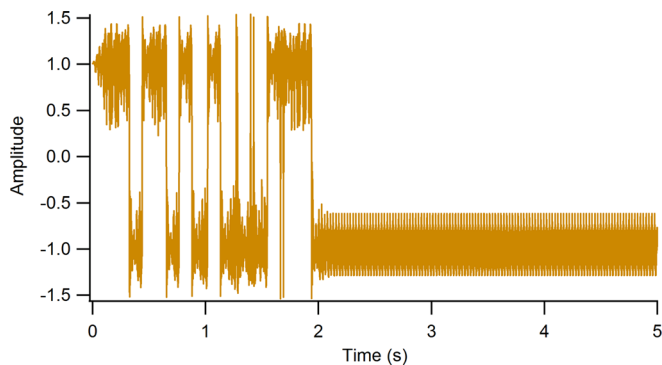


FIG. 6. On the low frequency side of the high power region, transient snap-through behavior can be observed before the system settles into a single well oscillation. This time series plots the equilibrium mode amplitude, with a forcing frequency of 39.7 Hz, and an available input power of 6 W.

before moving off to a stable period one orbit. Therefore, we see a high power output transient that settles to a low power output long term behavior. Presumably small perturbations to the system could result in returning to the high power non-attracting set through this region.

Though all of this bifurcation analysis has been developed at an available input power level of 6 W, these phenomena persist across the span of the high power region. Using AUTO to trace the bifurcation branches through the frequency/available power parameter space and plot them on top of the power output allows us to trace the boundaries of the high power region very accurately. Figure 7 shows this,

where saddle node branches are traced in black, period doubling branches in red, and the region of transient chaos highlighted in brown. Note that the region of transient chaos fills in the “bite” of low power output noted around 7–8 W of available input power. There is a high power lobe that occurs outside of the snap-through region on the low frequency side, between about 5 and 7 W of available input power. This is also traced by a saddle-node bifurcation, indicating that there is a sudden change from a low power output behavior to a high power output behavior.

**B. Periodic windows**

It is informative to examine the periodic windows that exist within the chaotic region. Reviewing Figure 3, we note that there are several windows where the period is quite high. By measuring the time elapsed between crossings of the equilibrium mode through zero in the positive direction, and averaging over a comparatively long time period we can define an average crossing frequency. Plotting this for a sweep at 6 W of available input power, and overlaying integer multiples of the forcing frequency produces Figure 8. Note that there are several regions where the frequency of the well-to-well oscillations is locked to the forcing frequency. This is particularly obvious in this figure between 40 and 40.5 Hz, where the oscillations are locked at 9 periods of the forcing cycle. Note also that Figure 3 indicates that the periodic windows exist at the same frequencies which indicate a lock between the forcing frequency and the response

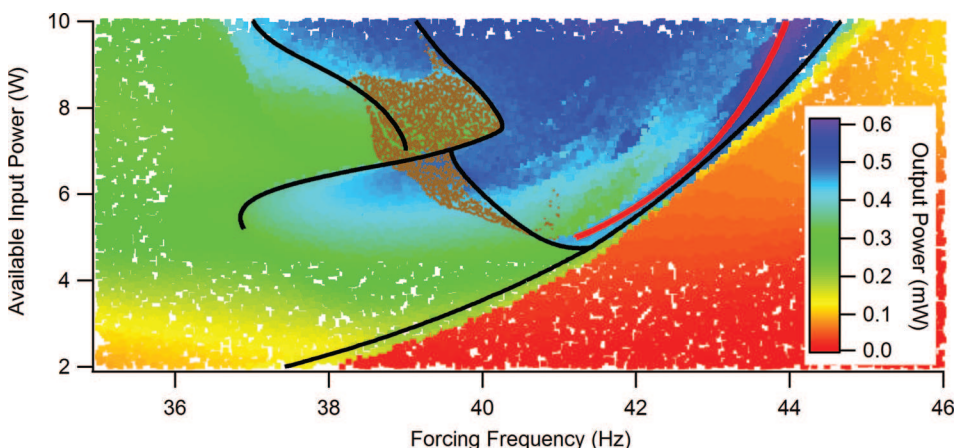


FIG. 7. Power output over the parameter space, with bifurcation sets shown. Black lines are associated with saddle-node bifurcations, and the red line is a period doubling bifurcation at the start of the period doubling cascade. The brown highlighting indicates regions of transient chaos. The majority of the high power output region is enclosed by the saddle-node bifurcations.

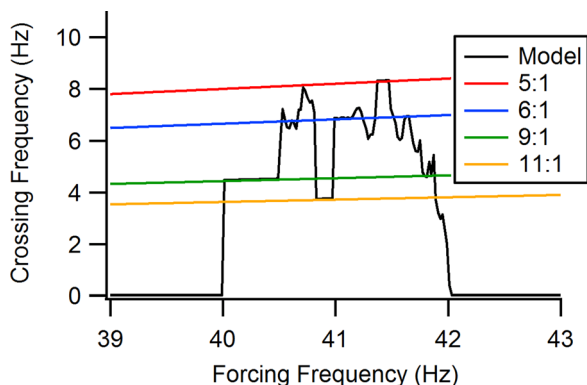


FIG. 8. Frequency locking in the well-to-well oscillation zone. Any time we are experiencing well-to-well oscillations, this frequency is non-zero. Note the regions where the crossing frequency locks to the forcing frequency. Locked oscillations of several different periods are present, ranging from 5 forcing cycles up to 11.

of the system. Moreover, the integer relation to the forcing frequency is coincident with the periodicity of the associated window. This phenomenon can be visualized through Figure 9, where the periodic windows have been highlighted in a color pattern consistent with their periodicity as determined from the locking behavior. In this plot, we have stacked multiple bifurcation diagrams together to give a sense of the development of the periodic windows and snap-through regions throughout the parameter space. Interestingly, we note that the relatively low period orbits only occur at higher power levels, with higher periodicities being present at lower available power levels. The expansion of the chaotic region with its interspersed periodic windows is clearly apparent from this perspective. The development of the chaotic region is closely associated with snap-through behavior, as evidenced by the fact that nearly all chaotic frequencies have strobe points in both wells. Therefore, it is reasonable to assume that for this beam, the chaotic attractor becoming stable results in high power output, though it is possible to achieve high power output without a chaotic attractor.

The transition between periodic and chaotic behavior within the chaotic attractor deserves some attention. A time series of a period 5 window with overlaid Poincaré map and a time series of a chaotic response very close in frequency is displayed in Figure 10. The phase portraits associated with each trajectory are also presented. The chaotic time series has sections that appear to behave in a very similar way to the periodic time series. However, there are intermittent bursts of aperiodic behavior that prevent the Poincaré map from repeating as it does in the periodic case. From this, it can be inferred that the transition between periodic behavior and chaotic behavior is governed by an intermittency transition around these periodic windows.

**IV. CONCLUSIONS**

Analysis of this beam model indicates that the presence of the chaotic attractor results in a relatively high power output. The chaotic attractor is associated with a period doubling cascade, an intermittency transition, and a crisis where an unstable period one orbit collides with the attractor. There

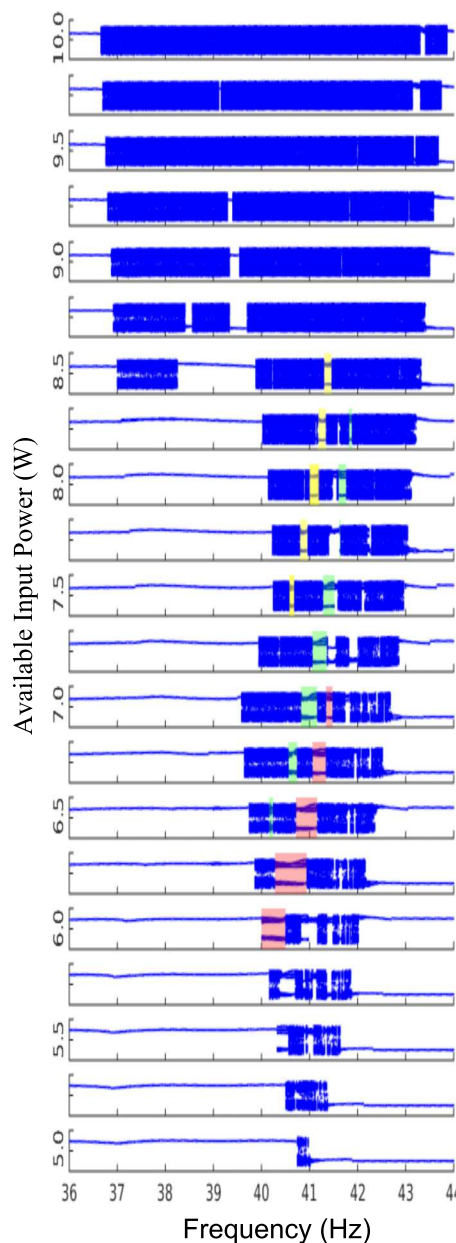


FIG. 9. Stacked bifurcation diagrams of the equilibrium mode show the evolution of the snap-through region. Here, some of the major periodic windows are highlighted: yellow corresponds to a period 5 oscillation, green to a period 9, and red to a period 7. As the available input power level is decreased, the trend is towards higher period periodic windows.

are regions where the power output increases without a chaotic attractor, but these areas are bounded by saddle-node bifurcations which are the start of a transformation of behavior which will result in a chaotic attractor when the parameter of interest continues to evolve. The resulting high power bandwidth is much greater than can be realized with a linear oscillator. This model performs quite well in comparison with other nonlinear energy harvesting devices, though the lack of a well defined and properly normalized performance metric for other studies makes quantitative comparison very difficult. Analysis of the single-forcing frequency model provides understanding of which transitions result in high power output, allowing models with different physical parameters

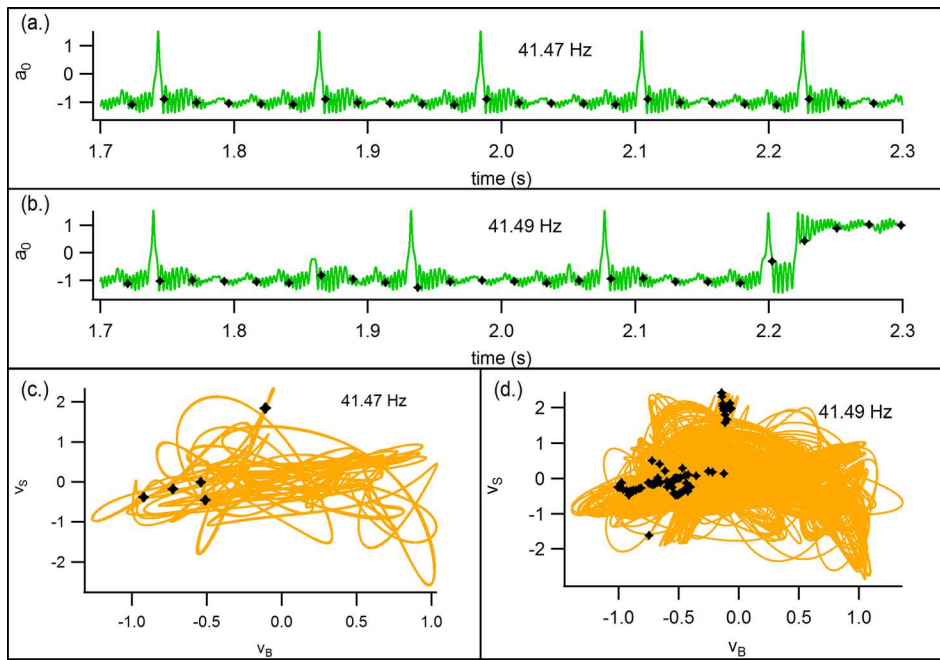


FIG. 10. Upper panels show time series of periodic response at 41.47 Hz, and chaotic response at 41.49 Hz. Lower panels phase space of period 5 oscillation at 41.47 Hz, and the response at 41.49 Hz where the Poincaré sections no longer form a periodic orbit. Note that the behavior of the chaotic series is very similar to the periodic response with bursts of different behavior interspersed that prevents the Poincaré map from repeating.

to be examined to determine how to go about optimizing the output power bandwidth, which is certainly an area worthy of further investigation.

#### ACKNOWLEDGMENTS

This work was supported by the National Science Foundation under Grant No. NSF-1131052.

<sup>1</sup>R. L. Harne and K. W. Wang, “A review of the recent research on vibration energy harvesting via bistable systems,” *Smart Mater. Struct.* **22**, 023001 (2013).

<sup>2</sup>A. J. Sneller, P. Cette, and B. P. Mann, “Experimental investigation of a post-buckled piezoelectric beam with an attached central mass used to harvest energy,” *J. Syst. Control Eng.* **225**, 497 (2011).

<sup>3</sup>F. Cottone, L. Gammaitoni, H. Vocca, M. Ferrari, and V. Ferrari, “Piezoelectric buckled beams for random vibration energy harvesting,” *Smart Mater. Struct.* **21**, 035021 (2012).

<sup>4</sup>L. Van Blarigan, J. Moehlis, and R. McMeeking, “Low dimensional modeling of a non-uniform, buckled piezoelectric beam for vibrational energy harvesting,” *Smart Mater. Struct.* **24**, 065012 (2015).

<sup>5</sup>See [www.advancedceramics.com](http://www.advancedceramics.com) for Beam parameters and commercial availability.

<sup>6</sup>L. Van Blarigan, P. Danzl, and J. Moehlis, “A broadband vibrational energy harvester,” *Appl. Phys. Lett.* **100**, 253904 (2012).

<sup>7</sup>Z. Levnajić and I. Mezić, “Ergodic theory and visualization. I. Mesochronic plots for visualization of ergodic partition and invariant sets,” *Chaos* **20**, 033114 (2010).

<sup>8</sup>E. Ott, *Chaos in Dynamical Systems* (Cambridge University Press, USA, 1994).

<sup>9</sup>See <http://cmvl.cs.concordia.ca/auto/> for AUTO user manual.

<sup>10</sup>F. C. Moon, *Chaotic Vibrations: An Introduction for Applied Scientists and Engineers* (Wiley, USA, 1987).

<sup>11</sup>P. Cvitanović, *Universality in Chaos* (CRC Press, USA, 1989).

<sup>12</sup>C. Grebogi, E. Ott, and J. A. Yorke, “Crises, sudden changes in chaotic attractors and transient chaos,” *Physica D* **7**, 181–200 (1983).

<sup>13</sup>A. Erturk and D. J. Inman, *Piezoelectric Energy Harvesting* (Wiley, UK, 2011).